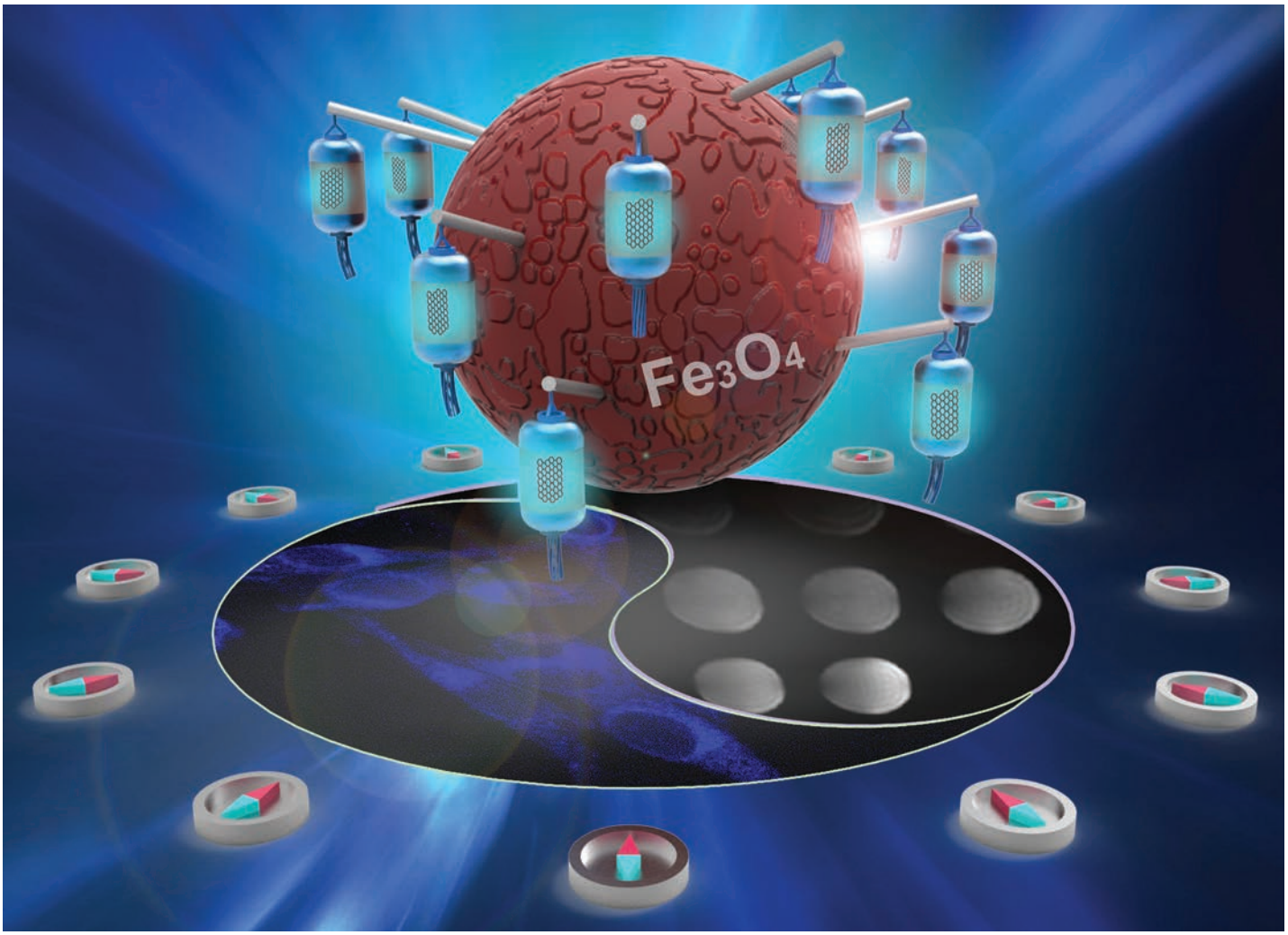

Showcasing research from the Professor Wenwu Qin labs at the Lanzhou University.

Title: One-pot synthesis of polyamines improved magnetism and fluorescence Fe_3O_4–carbon dots hybrid NPs for dual modal imaging

Magnetic–fluorescent hybrid nanoparticles Fe_3O_4–carbon dots were prepared through a one-step hydrothermal method from cheap and nontoxic materials. The prepared water-soluble Fe_3O_4–CDs hybrid NPs have a dual modal imaging ability for both MRI and fluorescent imaging.

As featured in:

See Wenwu Qin, Yunhuang Yang *et al*. *Dalton Trans*., 2016, **45**, 5484.

ROYAL SOCIETY OF CHEMISTRY

www.rsc.org/dalton

Registered charity number: 207890

Dalton Transactions

PAPER

View Article Online
View Journal | View Issue

Cite this: *Dalton Trans.*, 2016, **45**, 5484

One-pot synthesis of polyamines improved magnetism and fluorescence Fe_3O_4–carbon dots hybrid NPs for dual modal imaging†

Bo Li,[a,b] Xudong Wang,[a] Yali Guo,[a] Anam Iqbal,[a] Yaping Dong,[b] Wu Li,[b] Weisheng Liu,[a] Wenwu Qin,*[a] Shizhen Chen,[c] Xin Zhou[c] and Yunhuang Yang*[c]

Received 13th November 2015,
Accepted 1st January 2016

DOI: 10.1039/c5dt04488j

www.rsc.org/dalton

A one-step hydrothermal method was developed to fabricate Fe_3O_4–carbon dots (Fe_3O_4–CDs) magnetic–fluorescent hybrid nanoparticles (NPs). Ferric ammonium citrate (FAC) was used as a cheap and nontoxic iron precursor and as the carbon source. Moreover, triethylenetetramine (TETA) was used to improve the adhesive strength of CDs on Fe_3O_4 and the fluorescence intensity of CDs. The prepared water-soluble hybrid NPs not only exhibit excellent superparamagnetic properties (M_s = 56.8 emu g^{-1}), but also demonstrate excitation-independent photoluminescence for down-conversion and up-conversion at 445 nm. Moreover, the prepared water-soluble Fe_3O_4–CDs hybrid NPs have a dual modal imaging ability for both magnetic resonance imaging (MRI) and fluorescence imaging.

1. Introduction

The integration of multiple discrete components to construct multifunctional NPs combined with different unique functionalities from all individual components has received more and more attention due to their potential applications in many fields.[1–4] In particular, functionalized superparamagnetic NPs with fluorescence properties have attracted significant interest for their excellent potential in a wide variety of biomedical applications, such as magnetic resonance imaging (MRI), fluorescence imaging, drug delivery and photothermal therapy.[5–10] In order to construct magnetic–fluorescent hybrid NPs, tremendous efforts have been developed to combine magnetic and fluorescent materials into composite nano-functional materials that demonstrate properties of both components simultaneously. For example, core/shell and dumbbell-like structure magnetic–fluorescent hybrid NPs with a combination of noble metal NPs (Au or Ag NPs) or semiconducting quantum dots with superparamagnetic iron oxide have been synthesized, which show highly promising performance in the field of biomedical applications.[11–14] However, the preparation and use of conventional magnetic–fluorescent hybrid NPs in many practical applications has some limitations. For one thing, the fluorescent materials used, for instance organic dyes,[15,16] SQDs,[13,14] noble metal NPs,[11,12] and rare earth metal NPs,[17,18] have drawbacks such as poor photostability and biocompatibility, toxicity, and high cost. Furthermore, the complicated multi-step synthetic procedures for the preparation of these magnetic–fluorescent composite NPs are another obstruction for their practical applications.

Recently, CDs, a new type of fluorescence material, have been widely considered to be advantageous over other fluorescent materials due to their outstanding optical properties, high photostability, good aqueous solubility, low toxicity, and excellent biocompatibility.[19–21] Based on these superior properties, CDs are more suitable for use in optical bioimaging as fluorescent agents both *in vitro* and *in vivo* than traditional fluorescent materials. For example, Sun *et al.*[22] reported that CDs surface passivated by PPEI-EI exhibit strong luminescence with two-photon excitation in the near-infrared region, and the results of two-photon luminescence microscopy imaging of the CDs internalized in human breast cancer cells indicated the potential of the CDs in cell imaging with two-photon luminescence microscopy. Yang *et al.*[23] studied CDs for optical imaging *in vivo* firstly in 2009. The surface passivated CDs and CDs@ZnS were injected into mice through subcutaneous, interdermal and intravenous injections and remained strongly fluorescent *in vivo*. In addition, CDs can be easily obtained *via* various synthetic methods from a wide range of low-cost and

[a]*Key Laboratory of Nonferrous Metal Chemistry and Resources Utilization of Gansu Province Lanzhou University, Lanzhou, 730000 P. R. China. E-mail: qinww@lzu.edu.cn; Fax: +86 931-8912582*
[b]*Qinghai Institute of Salt Lakes, Chinese Academy of Sciences, Xining, Qinghai 810008, P. R. China*
[c]*Key Laboratory of Magnetic Resonance in Biological Systems, State Key Laboratory of Magnetic Resonance and Atomic and Molecular Physics, National Center for Magnetic Resonance in Wuhan, Wuhan Institute of Physics and Mathematics, Chinese Academy of Sciences, Wuhan 430071, China. E-mail: yang_yh@wipm.ac.cn*
†Electronic supplementary information (ESI) available. See DOI: 10.1039/c5dt04488j

available raw materials.[24–27] Citric acid, one of the most promising precursors for synthesizing CDs through the "bottom-up" method, is the most common choice. Yang *et al.*[28] reported a facile and high output strategy for fabricating CDs with a quantum yield (QY) as high as *ca.* 80% by condensing CA and ethylenediamine to form polymer-like CDs, followed by carbonization to form the CDs. Additionally, the relationship between their chemical structure and PL mechanism was investigated in detail. Li *et al.*[29] produced nitrogen and sulfur co-doped CDs (N, S-CDs) using CA as the carbon source and L-cysteine as a source of nitrogen and sulfur through a one-step hydrothermal treatment. The N, S-CDs exhibited very high QY (73%) and excitation-independent emission, resulting from the synergy effect of the doped nitrogen and sulfur atoms.

However, to the best of our knowledge, only a few hybrid NPs been reported that combined magnetic nanocrystals with CDs for dual-modal imaging.[30] Carbon dots possessing magnetism have been reported by us before.[31] The preparation of magnetic–fluorescent hybrid NPs (Ni@SiO_2–CDs) required lengthy multi-step synthetic procedures. Thus, the purpose of this work is to present a simple one pot method to synthesize magnetic–fluorescent hybrid NPs. In our synthetic strategy, ferric ammonium citrate (FAC) as a cheap and nontoxic iron precursor and carbon source and triethylenetetramine (TETA) are present in the reaction medium as reducing agent and nitrogen source, such that Fe(III) is reduced to form Fe_3O_4 NPs by TETA; meanwhile, citrate and TETA carbonize into nitrogen doped CDs. Finally, hybrid NPs based on magnetic iron oxide and fluorescent CDs can be obtained in one step conveniently. The obtained Fe_3O_4–CDs hybrid NPs not only show the superparamagnetic properties of the Fe_3O_4 nanocrystals for MRI contrast, but also manifest the compelling photoluminescence (PL) properties of the CDs, including excitation-independent emission and upconversion PL. The advantage of our preparation strategy in this study is the elimination of the tedious preparation of magnetic–fluorescent hybrid NPs. In addition, TETA is proved to be the major factor for the excellent properties of Fe_3O_4–CDs hybrid NPs by controlled trial. Therefore, these developed Fe_3O_4–CDs hybrid NPs are non-toxic and low cost, and should be ideal candidates for combined dual-modal imaging diagnosis.

2. Experimental

2.1 Materials and instruments

Ferric ammonium citrate (FAC) and triethylenetetramine (TETA, 70%) were purchased from Aladdin Reagent (Shanghai, China). Urea and citric acid monohydrate were purchased from Guangfu Reagent Company (Tianjin, China). Acetone was used as received without further purification. All reagents are Analytical Reagent grade. The water used in all experiments was deionized water prepared with Milli-Q water (18.2 MΩ cm).

XRD measurements were performed on an X-ray diffractometer (Philips X'Pert, Holland) with Cu Kα radiation (λ = 1.54059 Å), with operating voltage and current at 40 kV and 35 mA. X-ray photoelectron spectra (XPS) were acquired on a PHI 550 photoelectron spectrometer equipped with an Mg Kα X-ray source ($h\nu$ = 1253.6 eV). The X-ray gun operated at 15 kV and 20 mA. The background pressure of residual gases during the measurements was lower than 10^{-6} Pa. The transmission electron microscopy (TEM) was performed on a JEM-2100 transmission electron microscope at an acceleration voltage of 120 kV. Dynamic light scattering (DLS) was performed on a BI-200SM instrument (USA Brookhaven) at room temperature. Fourier transform infrared (FTIR) spectra were measured using a Nicolet 360 FTIR spectrometer with the KBr pellet technique. The magnetic behavior was tested using a vibrating sample magnetometer (VSM, Lake Shore 7304, Lake Shore, USA) at room temperature. UV-vis absorption spectra were obtained on an Agilent UV Cary100 spectrophotometer. An FLS920 spectrofluorometer was used to measure the steady-state emission spectra, fluorescence lifetimes and quantum yields. Quantum yields were determined by a relative method using quinine sulfate as the fluorescence standard. Fluorescence imaging was performed on an Olympus FV1000-IX81 laser confocal microscope. T_2-weighted MR images were acquired on a 7.0 T MRI scanner (Bruker BioSpec 70/20 USR), and R_2 values were measured on a Bruker 500 MHz NMR spectrometer.

2.2 Preparation of Fe_3O_4–CDs hybrid NPs

In a typical synthesis, AFC (0.133 g) was dissolved in H_2O and TETA 10 mL (volume ratio 9 : 1). The precursor solution was transferred to a 20 ml Teflon-lined stainless steel autoclave. After sealing, the autoclave was heated to and maintained at 200 °C for 2, 4 and 6 h. The autoclave was then cooled naturally to room temperature. The soliquid was separated by centrifugation (6500 rpm, 2 min) to discard the liquid phase. The obtained solid phase was dispersed in 10 ml acetone by ultrasonic dispersion for 3 minutes, and then separated magnetically. This washing process was repeated three times to remove dissociative CDs and TETA. Finally, the black products were dried in an air-circulating oven at 60 °C. By contrast, the synthesis was also performed without TETA. The samples are hereafter denoted as Fe_3O_4–CDs and Fe_3O_4, respectively.

2.3 *In vitro* MRI studies

Magnetic resonance imaging (MRI) tests were performed on a 7.0 T MRI scanner (Bruker BioSpec 70/20 USR). Fe_3O_4–CDs NPs were dispersed in deionized water with various concentrations, and then 200 μL samples were placed into a 96-well plate. The T_2-weighted images were acquired using the multi-slice-multi-echo sequence (MSME) with the following parameters: echo time = 100 ms, repetition time = 2000 ms, field of view = 2 × 2 cm^2, number of average = 1, matrix size = 128 × 96 (data zero filled to a 256 × 256 matrix).

The R_2 values of the Fe_3O_4–CDs NPs were measured using the Carr-Purcell-Meiboom-Gill (CPMG) sequence with a broadband decoupling inverse 1H probe (BBI) on a Bruker 500 MHz NMR spectrometer. Fe_3O_4–CDs NPs were dispersed in 98% deuterium oxide with various concentrations and then 500 μL was taken into 5 mm sample tubes.

2.4 Cell culture, fluorescence imaging and cytotoxicity assay

Cellular fluorescence images were recorded using an Olympus FV1000-IX81 laser confocal microscope. BHK cells were cultured in DMEM (Dulbecco's Modified Eagle's Medium) supplemented with 10% FBS (fetal bovine serum). The cell lines were maintained under a humidified atmosphere containing 5% CO_2 at 37 °C. After the removal of the culture medium, the cells were incubated with 200 μg ml^{-1} Fe_3O_4–CDs hybrid NPs in 1.0 ml of fresh culture medium for 2 h. The cells were washed three times with PBS to remove the residual nanoparticles before the imaging measurements.

Cytotoxicity test. BHK cells were seeded at a density of 10^4 cells per well (100 μL total volume per well) in 96-well assay plates for 24 h. Then the as-prepared Fe_3O_4–CDs hybrid NPs were added to the cell culture medium at the indicated concentrations (20, 40, 80, 160, 200 μg mL^{-1}). The cells were incubated with Fe_3O_4–CDs for 24 h. To determine toxicity, 3-(4,5-dimethylthiazol-2-yl)-5-(3-carboxymethoxyphenyl)-2-(4-sulfophenyl)-2*H*-tetrazolium, inner salt (MTS), was added to each well of the microtiter plate, and the plate was incubated in a CO_2 incubator for an additional 4 h. The absorbance values were determined with a Bio-Rad model-680 microplate reader at 490 nm (corrected for background absorbance at 630 nm). The cell viability was estimated according to the following equation: cell viability (%) = mean of the absorbance value of the treatment group/mean absorbance value of the control × 100%.

3. Results and discussion

The Fe_3O_4–CDs hybrid NPs were synthesized by a one-step hydrothermal method. The obtained Fe_3O_4–CDs hybrid NPs exhibit good water solubility and show bright blue luminescence under excitation of a 365 nm UV lamp in water. However, the product synthesized without TETA has no luminescence under the same conditions, because the CDs produced during the synthesis process were washed away by acetone from the surface of Fe_3O_4.

3.1 Physical structure of Fe_3O_4–CDs

Fig. 1 gives the results of XRD analysis of the obtained nanoparticles under different hydrothermal times and solution environments. The reflections of 111, 220, 311, 400, 422, 511 and 440 in the typical XRD pattern can be matched well with standard magnetic Fe_3O_4, according to JCPDS card No. 19-0629. Obviously, the degree of crystallinity of the samples synthesized with TETA (a, b, c) is better than those synthesized without TETA (d, e, f) and increases with hydrothermal time. This result demonstrates that TETA and longer hydrothermal times are beneficial to produce well-crystallized Fe_3O_4 nanoparticles by hydrothermal techniques. This improvement due to using hydrophilic TETA in the synthesis of iron oxide NPs was observed in a previous study.[32] It is believed that TETA provides a reductive environment to partially reduce the iron precursors and facilitate the nucleation and subsequent

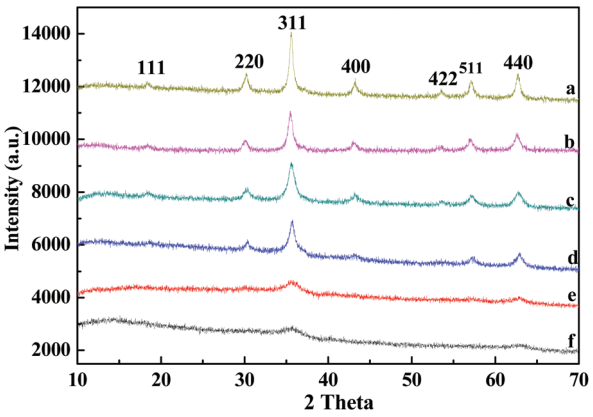

Fig. 1 XRD patterns of Fe_3O_4–CDs and Fe_3O_4: a, b, and c are Fe_3O_4–CDs with hydrothermal times of 6 h, 4 h, and 2 h; d, e, and f are Fe_3O_4 with hydrothermal times of 6 h, 4 h, and 2 h.

growth period. The reason that no typical reflection of CDs in 20–25° was detected for the Fe_3O_4–CDs hybrid NPs may be the relatively low content and poor crystallinity of the CDs in Fe_3O_4–CDs hybrid NPs. The XRD pattern of TETA–CDs obtained by a hydrothermal time of 6 h at 200 °C is given in Fig. S1;† a broad diffraction peak centered at 2θ = 23° (d_{002} = 0.31 nm) is detected, as in other reports.[29,33]

Fig. 2 shows the typical transmission electron microscopy (TEM) images of Fe_3O_4 and Fe_3O_4–CDs hybrid NPs with a hydrothermal time of 6 h. The TEM image (Fig. 2A) shows that the Fe_3O_4 NPs appear irregular in morphology and size ranging from several nanometers to tens of nanometers. In contrast, the Fe_3O_4–CDs hybrid NPs (Fig. 2B) possess rather uniform particle morphology and size. The result of dynamic light scattering (DLS) measurement (inset of Fig. 2B) shows that the size of Fe_3O_4–CDs hybrid NPs is distributed in the range from 9 to 13 nm, with an average size of 12 nm. These results, together with the XRD analysis, indicate that TETA plays a critical role in modifying the particle and crystallite characteristics. The high-resolution TEM (HRTEM) image (Fig. 2C) reveals the high crystallinity of the Fe_3O_4–CDs hybrid NPs. The lattice spacing of 0.32 nm should be the spacing between the graphene layers (002 facet) which is similar to that of many other reported CDs.[29,34–36] The interplanar spacing at about 0.25 nm and 0.29 nm correspond to the (3 1 1) and (2 2 0) lattice planes of the cubic Fe_3O_4 (0.253 nm and 0.297 nm), respectively. To further confirm the formation of the composite structure, energy dispersive X-ray spectroscopy (EDS) element mapping was recorded and is shown in Fig. 2E. The (EDS) element mapping clearly shows that the elements of Fe, O, C and N are evenly distributed in the Fe_3O_4–CDs hybrid NPs. It can be seen from the (EDS) element mapping results that the CDs have good dispersivity with Fe_3O_4 particles. The morphology of the TETA–CDs were also characterized by TEM and dynamic light scattering (DLS) measurements, as shown in Fig. 2D. The size of the as prepared TETA–CDs is distributed in the range from 1 to 3 nm, with an average size of 2 nm.

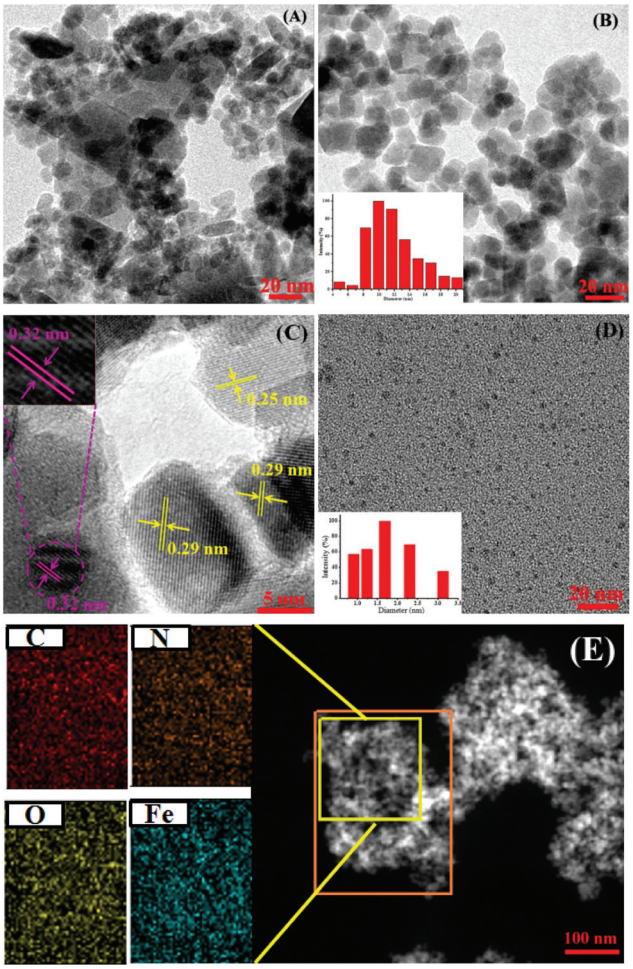

Fig. 2 TEM images of Fe_3O_4 (A), Fe_3O_4–CDs and size distribution histogram (inset) (B), HRTEM image of Fe_3O_4–CDs and enlarged selection area (inset) (C), TEM image of as-prepared TETA–CDs with a hydrothermal time of 6 h at 200 °C and size distribution histogram (inset) (D), and EDS element mapping data of Fe, O, C and N elements throughout the Fe_3O_4–CDs (E).

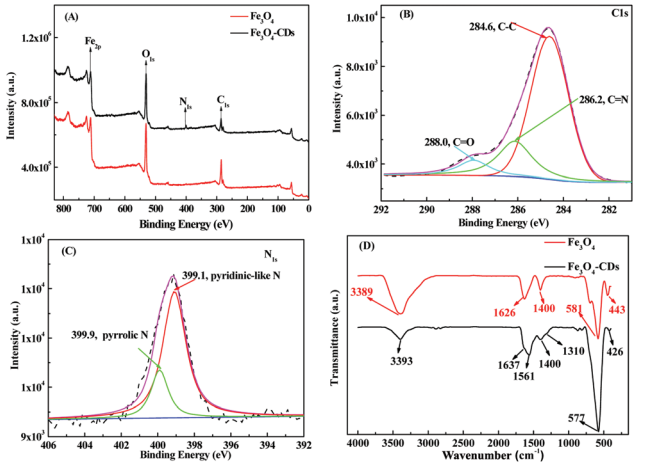

Fig. 3 XPS full-scan spectra of Fe_3O_4 and Fe_3O_4–CDs NPs (A), XPS high resolution survey scan of (B) C 1s and (C) N 1s region of Fe_3O_4–CDs NPs; (D) FT-IR spectra of Fe_3O_4 and Fe_3O_4–CDs NPs.

3.2 Chemical structure of Fe_3O_4–CDs

X-ray photoelectron spectra (XPS) were employed to investigate the surface composition of the as prepared Fe_3O_4–CDs and Fe_3O_4 NPs. Fig. 3A presents the XPS full-scan spectra of the Fe_3O_4–CDs and Fe_3O_4 NPs. Obviously, the XPS spectra indicate that both the Fe_3O_4–CDs and Fe_3O_4 NPs are composed of iron, oxygen and carbon. However, nitrogen is detected only in the Fe_3O_4–CDs hybrid NPs. The high-resolution spectrum of C 1s of the Fe_3O_4–CDs hybrid NPs (Fig. 3B) can be de-convoluted into three peaks at 284.6, 286.2, and 288.0 eV, assigned to carbon in the form of C–C, C=N and C=O, respectively.[29,37] The N 1s high-resolution spectrum (Fig. 3C) displays two peaks at 399.2 and 400.6, indicating that nitrogen exists mostly in the form of pyridinic-like N and pyrrolic-like N.[37]

To further confirm the chemical composition of the Fe_3O_4–CDs, FT-IR spectra were recorded to identify the functional groups. As given in Fig. 3D, the main bands of the Fe_3O_4 NPs at 3389 cm^{-1}, 1626 cm^{-1}, and 1400 cm^{-1} can be assigned to the O–H stretching vibration, C=O stretching vibration, and C–O bending vibration, respectively; the bands at 581 cm^{-1} and 443 cm^{-1} are attributed to the Fe–O bonds.[38] The intense band at 1626 cm^{-1} for Fe_3O_4 NPs reveals the binding of a CA radical to surface of the Fe_3O_4 NPs. CA as a coordinating ligand could stabilize the Fe_3O_4 NPs to some extent, but would not influence the magnetic properties and would hardly immobilize the CDs on the surface of Fe_3O_4 NPs. For the Fe_3O_4–CDs, the band at 3393 cm^{-1} indicates the existence of O–H and N–H. The broader band at 1561 cm^{-1} with a shoulder about 1637 cm^{-1} may be due to the N–H bending vibration and the amide I C=O stretching vibration.[39] The weak band at 1310 cm^{-1} is assigned to the C–N stretching vibration. The bands at 1400 cm^{-1}, 577 cm^{-1} and 426 cm^{-1} refer to the C–O bond and the Fe–O bonds respectively, as in Fe_3O_4. Both the XPS and FT-IR spectra results indicate that N doped CDs were synthesized with TETA and attached on the surface of Fe_3O_4 nanoparticles.

3.3 Magnetic and optical properties of Fe_3O_4–CDs

The magnetic properties of the Fe_3O_4–CDs and Fe_3O_4 NPs were measured at room temperature with a vibrating sample magnetometer (VSM). Fig. 4 shows the magnetization of magnetite nanocrystals prepared under different solution conditions and hydrothermal times. The saturation magnetizations of Fe_3O_4–CDs with hydrothermal times of 2 h, 4 h, and 6 h are 43.2, 50.6, and 56.8 emu g^{-1}, respectively, which are much higher than the best result for Fe_3O_4 of 23.7 emu g^{-1} with 6 h hydrothermal time. The saturation magnetization of the Fe_3O_4–CDs does not decrease compared to unhybridized Fe_3O_4, in contrast to previously reported magnetic composite materials.[31,40] The great gap in saturation magnetization between the Fe_3O_4–CDs and Fe_3O_4 should be mainly attributed to the better crystallinity attributed to the improvement of TETA, as shown in

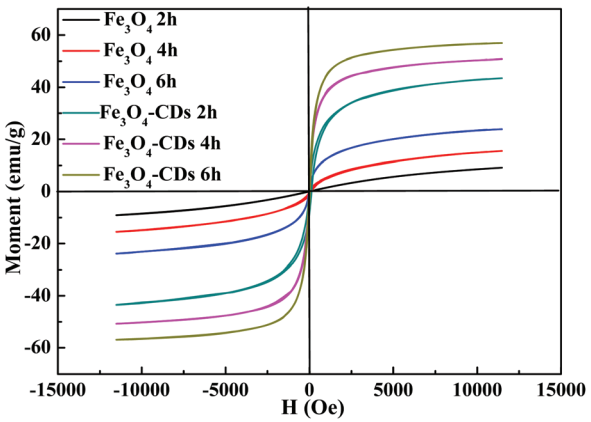

Fig. 4 Room-temperature magnetization curves of Fe_3O_4–CDs and Fe_3O_4 at different hydrothermal times.

Fig. 1. Also, the longer hydrothermal time also effectively promoted the magnetism of the Fe_3O_4–CDs and Fe_3O_4 by increasing crystallinity as well.

Fig. 5 shows UV-vis absorption spectra of TETA–CDs, Fe_3O_4–CDs and Fe_3O_4 in aqueous solution; the inset shows corresponding photographs taken under daylight and UV lamp. The TETA–CDs show two typical absorption peaks at 242 and 354 nm. The peak at 242 nm is ascribed to the π–π* transition of the C=C band, and the other peak at about 354 nm derives from the trapping of excited state energy by the surface states, leading to a strong FL signal.[29] The absorption of Fe_3O_4–CDs also shows two obvious absorption peaks at the same wavelength, while the absorption of Fe_3O_4 has no obvious absorption peaks in the UV-vis light area. This result indicates that CDs retain good photoresponse in the UV-vis region, similar to that of the TETA–CDs, which is unaffected by iron ion in the synthetic process. In addition, introducing TETA effectively improves the adhesion of Fe_3O_4 and CDs due to the presence of amines on the surface of the CDs. The UV-vis absorption spectra of the CA–CDs and N–CDs in an aqueous solution are shown in Fig. S2.† The N–CDs have two absorption peaks at 235 and 335 nm which are blue-shifted relative to the corresponding absorption peaks of the TETA–CDs. However, the CA–CDs have no obvious absorption peaks in the UV-vis light area.

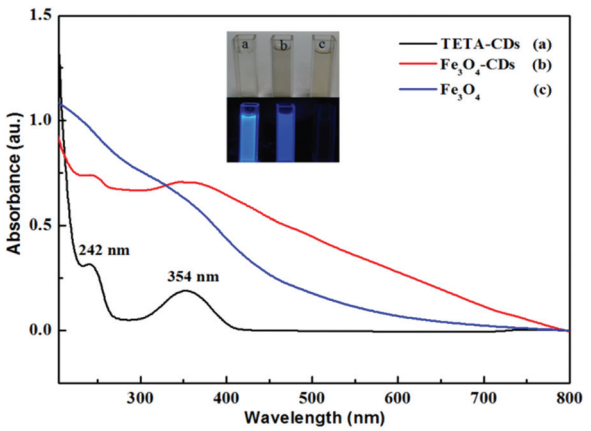

Fig. 5 UV-vis absorption spectra of TETA–CDs, Fe_3O_4–CDs and Fe_3O_4 in water. The inset shows the samples under daylight and UV lamp (the excitation wavelength is 365 nm).

The photoluminescence properties of the Fe_3O_4–CDs were examined in water at different excitation wavelengths, as shown in Fig. 6A. Unlike most CDs, the emission wavelength of the Fe_3O_4–CDs at 445 nm hardly shifted as the excitation wavelength changed from 300 nm to 410 nm. The maximum excitation wavelength of Fe_3O_4–CDs aqueous solution is 360 nm. The emission wavelength of the TETA–CDs is also excitation independent, with maximum excitation wavelengths and fixed emission wavelengths of 370 nm and 445 nm respectively, as illustrated in Fig. S3A.† This result indicates that the CDs in Fe_3O_4–CDs hybrid NPs may have the same mechanism of luminescence as the TETA–CDs. However, the FL quantum yield (FLQY) of Fe_3O_4–CDs decreased dramatically in contrast with that of the TETA–CDs. The FL quantum yield of the TETA–CDs is about 53% when excited with 360 nm light, while the FL quantum yield of Fe_3O_4–CDs is only about 4.6%. The acute quenching of the Fe_3O_4–CDs is due to static and dynamic fluorescence quenching of the dots and strong absorption of the transmitted light by the iron oxide particles, as shown in Fig. 5.[41]

The up-conversion PL properties of the Fe_3O_4–CDs and TETA–CDs were also investigated, as shown in Fig. 6B and S3B.† The up-conversion PL spectra show a fixed emission peak at the same wavelength of 445 nm as the down-conversion PL spectra and remain unchanged when the excitation wavelength varies, which indicates that the emission occurs from the lowest single state regardless of the mode of excitation, as observed in microwave-assisted synthesized DEG-CDs.[33] However, the photoluminescence properties of the CA–CDs and N–CDs are different from those of the Fe_3O_4–CDs and TETA–CDs. The emission wavelengths of the CA–CDs and N–CDs are excitation dependent, including down-conversion and up-conversion, as shown in Fig. S4 and S5.† These results imply that TETA not only acts as a nitrogen source for CDs synthesis with CA but also helps to form a relatively uniform surface status.[29]

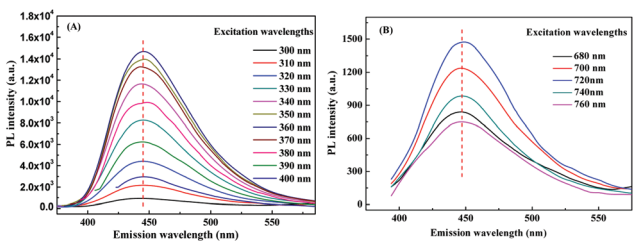

Fig. 6 Fluorescence spectra of Fe_3O_4–CDs at different excitation wavelengths: (A) down-conversion and (B) up-conversion.

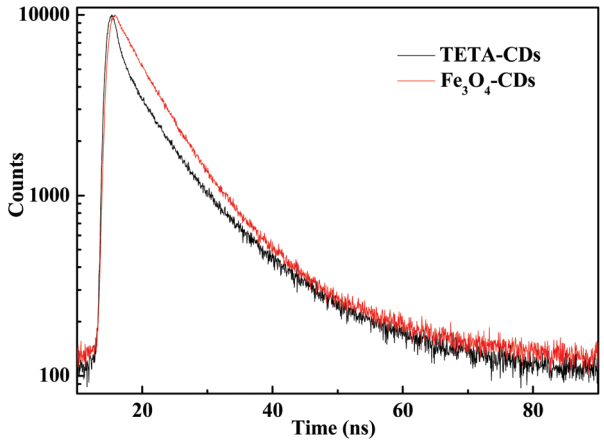

Fig. 7 The decay curves of Fe_3O_4–CDs and TETA–CDs in an aqueous solution, collected at 440 nm with excitation at 360 nm.

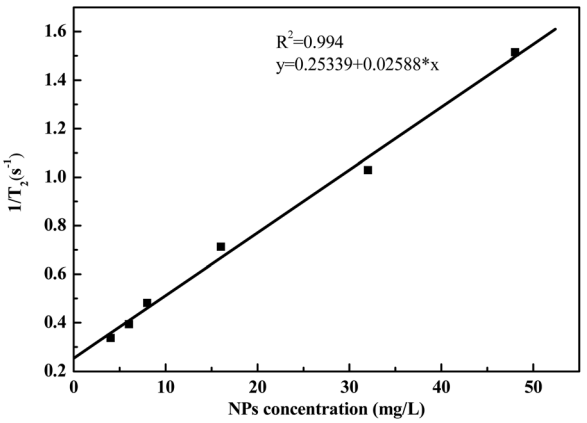

Fig. 9 Plot of R_2 values of the Fe_3O_4–CDs NPs.

To investigate the fluorescence dynamics of the Fe_3O_4–CDs and TETA–CDs, fluorescence decay traces of the Fe_3O_4–CDs and TETA–CDs were recorded at three emission wavelengths (440 nm, 460 nm and 480 nm) by the single-photon timing method. The fluorescence decays for the Fe_3O_4–CDs and TETA–CDs aqueous solution were studied as shown in Fig. 7 and Table S1.†

The fluorescence decay of TETA–CDs aqueous solution at λ_{ex} = 360 nm can be described as tri-exponential function with the contributions of the τ_1 (~14 ns, 39%), τ_2 (~5 ns, 46%) and τ_3 (~0.8 ns, 15%). The multiexponential nature of the lifetime suggests that the components of TETA–CDs in water are complicated, probably due to the involvement of different particle sizes and emissive trap sites. Meanwhile, the fluorescence decay of Fe_3O_4–CDs aqueous solution can be described as a bi-exponential function with the contributions of τ_1 (~13 ns, 34%) and τ_2 (~5 ns, 66%) at the same excitation wavelength λ_{ex} = 360 nm. The presence of Fe_3O_4 in the TETA–CDs does not change the two longer fluorescence lifetimes (~14 ns and ~5 ns) of the TETA–CDs.

3.4 *In vitro* MRI

In order to evaluate the T_2 contrast properties of the Fe_3O_4–CDs NPs, T_2-weighted images of the as-prepared NPs dispersed in deionized water with different concentrations (I, 2 μg mL^{-1}; II, 4 μg mL^{-1}; III, 6 μg mL^{-1}; IV, 8 μg mL^{-1}; V, 16 μg mL^{-1}; VI, 32 μg mL^{-1}; VII, 48 μg mL^{-1}) were obtained in a Bruker Biospec 7.0T MRI system at room temperature. It can be clearly seen that the signal intensity of the MR images is related to the concentration of Fe_3O_4–CDs NPs (Fig. 8). The r_2 value of the Fe_3O_4–CDs NPs was r_2 = 0.02588 mL μg^{-1} s^{-1}, measured in a Bruker 500 MHz NMR spectrometer (Fig. 9). Those results indicate that the as-prepared Fe_3O_4–CDs NPs could be used as a T_2 contrast agent in MRI.

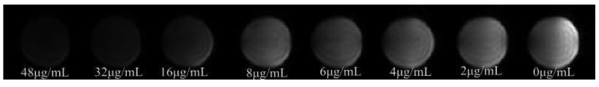

Fig. 8 T_2-weighted MR images of Fe_3O_4–CDs at various concentrations at 7 T.

3.5 Cell imaging

It is expected that the Fe_3O_4–CDs hybrid NPs should have a dual modal imaging ability for both MRI and fluorescence imaging. For living cell labeling and imaging, the bioimaging properties of Fe_3O_4–CDs using a confocal microscope with BHK cells was performed. BHK cells loaded with Fe_3O_4–CDs for 2 h at 37 °C show bright blue luminescence when excited with 365 nm UV light, as shown in Fig. 10. The laser scanning confocal images clearly indicate that the Fe_3O_4–CDs can transfer into living cells. The results suggest that the Fe_3O_4–CDs have great application potential in multimodal bioimaging, with the fluorescence imaging ability of the CDs and the superparamagnetism ability of the Fe_3O_4. In addition, cell cytotoxicity experiments with the Fe_3O_4–CDs hybrid NPs were evaluated using BHK cell lines through the MTS assay. As shown in Fig. S7,† the Fe_3O_4–CDs exhibited low cytotoxicity, which may be due to the low toxicity of the CDs.

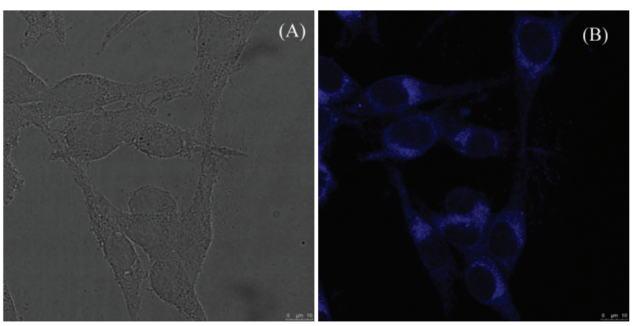

Fig. 10 Fluorescence image of BHK cells incubated with 200 μg ml^{-1} of Fe_3O_4–CDs. The bright-field image (A) and the confocal fluorescence image (B).

4. Conclusions

In summary, magnetic–fluorescent Fe_3O_4–CDs hybrid NPs have been synthesized from precursor ferric ammonium citrate and triethylenetetramine through a simple one-pot hydrothermal route. The advantage of our preparation strategy is that the synthesis eliminates the tedious preparation of magnetic–fluorescent hybrid NPs. The excellent superparamagnetic and excitation-independent emission properties in water of the Fe_3O_4–CDs hybrid NPs give them great potential for applications in multimodal bioimaging. In addition, triethylenetetramine is proved as major factor for the excellent properties of Fe_3O_4–CDs hybrid NPs and excitation-independent emission properties of CDs by controlled trial.

Acknowledgements

This study was supported by the National Science Foundation for Fostering Talents in Basic Research of the National Natural Science Foundation of China (Grant No. J1103307). The authors would like to thank the Natural Science Foundation of China (No. 21271094, 21305156, 21575155). Y. Yang would like to thank the Hundred Talent Program by Chinese Academy of Sciences.

Notes and references

1 E. Roy, S. Patra, D. Kumar, R. Madhuri and P. K. Sharma, *Biosens. Bioelectron.*, 2015, **68**, 726–735.
2 X. L. Qiu, Q. L. Li, Y. Zhou, X. Y. Jin, A. D. Qi and Y. W. Yang, *Chem. Commun.*, 2015, **51**, 4237–4240.
3 L. Huang, L. Ao, W. Wang, D. Hu, Z. Sheng and W. Su, *Chem. Commun.*, 2015, **51**, 3923–3926.
4 Y. Chen, K. Ai, J. Liu, G. Sun, Q. Yin and L. Lu, *Biomaterials*, 2015, **60**, 111–120.
5 C. Tudisco, M. T. Cambria, F. Sinatra, F. Bertani, A. Alba, A. E. Giuffrida, S. Saccone, E. Fantechi, C. Innocenti, C. Sangregorio, E. Dalcanale and G. G. Condorelli, *J. Mater. Chem. B*, 2015, **3**, 4134–4145.
6 J. Shen, Y. Li, Y. Zhu, X. Yang, X. Yao, J. Li, G. Huang and C. Li, *J. Mater. Chem. B*, 2015, **3**, 2873–2882.
7 K. Yang, L. Hu, X. Ma, S. Ye, L. Cheng, X. Shi, C. Li, Y. Li and Z. Liu, *Adv. Mater.*, 2012, **24**, 1868–1872.
8 Z. Fan, M. Shelton, A. K. Singh, D. Senapati, S. A. Khan and P. C. Ray, *ACS Nano*, 2012, **6**, 1065–1073.
9 L. Cheng, K. Yang, Y. Li, X. Zeng, M. Shao, S.-T. Lee and Z. Liu, *Biomaterials*, 2012, **33**, 2215–2222.
10 L. Cheng, K. Yang, Y. Li, J. Chen, C. Wang, M. Shao, S. T. Lee and Z. Liu, *Angew. Chem., Int. Ed.*, 2011, **123**, 7523–7528.
11 J. Jiang, H. Gu, H. Shao, E. Devlin, G. C. Papaefthymiou and J. Y. Ying, *Adv. Mater.*, 2008, **20**, 4403–4407.
12 Z. Xu, Y. Hou and S. Sun, *J. Am. Chem. Soc.*, 2007, **129**, 8698–8699.
13 S. Selvan, P. K. Patra, C. Y. Ang and J. Y. Ying, *Angew. Chem., Int. Ed.*, 2007, **119**, 2500–2504.
14 H. Gu, R. Zheng, X. Zhang and B. Xu, *J. Am. Chem. Soc.*, 2004, **126**, 5664–5665.
15 S. K. Yen, D. Janczewski, J. L. Lakshmi, S. B. Dolmanan, S. Tripathy, V. H. Ho, V. Vijayaragavan, A. Hariharan, P. Padmanabhan and K. K. Bhakoo, *ACS Nano*, 2013, **7**, 6796–6805.
16 J. E. Lee, N. Lee, H. Kim, J. Kim, S. H. Choi, J. H. Kim, T. Kim, I. C. Song, S. P. Park and W. K. Moon, *J. Am. Chem. Soc.*, 2009, **132**, 552–557.
17 H. Zhu, J. Tao, W. Wang, Y. Zhou, P. Li, Z. Li, K. Yan, S. Wu, K. W. Yeung and Z. Xu, *Biomaterials*, 2013, **34**, 2296–2306.
18 H. Zhu, Y. Shang, W. Wang, Y. Zhou, P. Li, K. Yan, S. Wu, K. W. Yeung, Z. Xu and H. Xu, *Small*, 2013, **9**, 2991–3000.
19 X. T. Zheng, A. Ananthanarayanan, K. Q. Luo and P. Chen, *Small*, 2015, **11**, 1620–1636.
20 S. Ray, A. Saha, N. R. Jana and R. Sarkar, *J. Phys. Chem. C*, 2009, **113**, 18546–18551.
21 Y.-P. Sun, B. Zhou, Y. Lin, W. Wang, K. S. Fernando, P. Pathak, M. J. Meziani, B. A. Harruff, X. Wang and H. Wang, *J. Am. Chem. Soc.*, 2006, **128**, 7756–7757.
22 L. Cao, X. Wang, M. J. Meziani, F. Lu, H. Wang, P. G. Luo, Y. Lin, B. A. Harruff, L. M. Veca, D. Murray, S.-Y. Xie and Y.-P. Sun, *J. Am. Chem. Soc.*, 2007, **129**, 11318–11319.
23 S.-T. Yang, L. Cao, P. G. Luo, F. Lu, X. Wang, H. Wang, M. J. Meziani, Y. Liu, G. Qi and Y.-P. Sun, *J. Am. Chem. Soc.*, 2009, **131**, 11308–11309.
24 S. Sahu, B. Behera, T. K. Maiti and S. Mohapatra, *Chem. Commun.*, 2012, **48**, 8835–8837.
25 X. Wang, K. Qu, B. Xu, J. Ren and X. Qu, *J. Mater. Chem.*, 2011, **21**, 2445–2450.
26 Q. Wang, H. Zheng, Y. Long, L. Zhang, M. Gao and W. Bai, *Carbon*, 2011, **49**, 3134–3140.
27 F. Wang, S. Pang, L. Wang, Q. Li, M. Kreiter and C.-Y. Liu, *Chem. Mater.*, 2010, **22**, 4528–4530.
28 S. Zhu, Q. Meng, L. Wang, J. Zhang, Y. Song, H. Jin, K. Zhang, H. Sun, H. Wang and B. Yang, *Angew. Chem., Int. Ed.*, 2013, **125**, 4045–4049.
29 Y. Dong, H. Pang, H. B. Yang, C. Guo, J. Shao, Y. Chi, C. M. Li and T. Yu, *Angew. Chem., Int. Ed.*, 2013, **52**, 7800–7804.
30 Z. Markova, A. B. Bourlinos, K. Safarova, K. Polakova, J. Tucek, I. Medrik, K. Siskova, J. Petr, M. Krysmann, E. P. Giannelis and R. Zboril, *J. Mater. Chem.*, 2012, **22**, 16219–16223.
31 D. Wang, Y. Guo, W. Liu and W. Qin, *RSC Adv.*, 2014, **4**, 7435–7439.
32 H. Qu, H. Ma, A. Riviere, W. Zhou and C. J. O'Connor, *J. Mater. Chem.*, 2012, **22**, 3311–3313.
33 Y. Liu, N. Xiao, N. Gong, H. Wang, X. Shi, W. Gu and L. Ye, *Carbon*, 2014, **68**, 258–264.
34 Y. Xu, M. Wu, Y. Liu, X. Z. Feng, X. B. Yin, X. W. He and Y. K. Zhang, *Chem. – Eur. J.*, 2013, **19**, 2276–2283.
35 Z. C. Yang, M. Wang, A. M. Yong, S. Y. Wong, X. H. Zhang, H. Tan, A. Y. Chang, X. Li and J. Wang, *Chem. Commun.*, 2011, **47**, 11615–11617.

36 H. Ding, J. S. Wei and H. M. Xiong, *Nanoscale*, 2014, **6**, 13817–13823.
37 Y.-Q. Zhang, D.-K. Ma, Y. Zhuang, X. Zhang, W. Chen, L.-L. Hong, Q.-X. Yan, K. Yu and S.-M. Huang, *J. Mater. Chem.*, 2012, **22**, 16714–16718.
38 S. Nigam, K. C. Barick and D. Bahadur, *J. Magn. Magn. Mater.*, 2011, **323**, 237–243.
39 C. Liu, P. Zhang, X. Zhai, F. Tian, W. Li, J. Yang, Y. Liu, H. Wang, W. Wang and W. Liu, *Biomaterials*, 2012, **33**, 3604–3613.
40 Y. Xu, A. Karmakar, D. Wang, M. W. Mahmood, F. Watanabe, Y. Zhang, A. Fejleh, P. Fejleh, Z. Li and G. Kannarpady, *J. Phys. Chem. C*, 2010, **114**, 5020–5026.
41 S. A. Corr, Y. P. Rakovich and Y. K. Gun'ko, *Nanoscale Res. Lett.*, 2008, **3**, 87–104.